Met. Mater. Int., Vol. 21, No. 1 (2015), pp. 14~21
doi: 10.1007/s12540-015-1003-y

Effect of Applied Potential on Fatigue Crack Propagation Behavior of Fe24Mn Steel in Seawater

Daeho Jeong[1], Soongi Lee[2], Insik Seo[2], Jangyong Yoo[2], and Sangshik Kim[1,*]

[1]Department of Materials Science and Engineering, ReCAPT, Gyeongsang National University, Chinju 660-701, Korea
[2]Plate Research Group, Technical Research Laboratory, POSCO, Pohang 790-785, Korea

(received date: 21 March 2014 / accepted date: 24 April 2014)

The fatigue crack propagation (FCP) tests were conducted on Fe24Mn steel in the region of base metal (BM) and weld metal (WM), in air and artificial seawater (ASW) under various applied potentials to establish optimum and safe working limits of cathodic protection (CP). The CP potential of -850 and -1,050 mV_{SCE} suppressed the environmental effect of seawater on the FCP behavior of Fe24Mn BM and WM specimens, showing almost identical da/dN-ΔK curves for both air and ASW environments. The slow strain rate tests were also conducted on the Fe24Mn BM specimen in ASW under the CP potential of -1,050 mV_{SCE} to identify the susceptibility of hydrogen affecting the FCP behavior. It was suggested that the Fe24Mn BM specimen steel is susceptible to hydrogen embrittlement, but the effect of hydrogen was marginal in affecting the FCP behavior of the Fe24Mn specimens at a loading frequency of 10 Hz. The FCP behavior of Fe24Mn steel is discussed based on the fractographic observation to understand the FCP mechanism in seawater under various CP potentials.

Keywords: alloys, welding, fatigue, artificial seawater, show strain rate test

1. INTRODUCTION

The austenitic stainless steels are widely used engineering alloys in harsh environments, such as seawater and cryogenic temperatures [1,2]. They have excellent corrosion resistance and good toughness and fatigue resistance [3,4], but suffering from low yield strength and high price [5-9]. As low cost and high strength substitute for the present austenitic steels, there is a great deal of research interest on high manganese (Mn) steels particularly for offshore applications [10,11]. POSCO, for example, has been developing a variety of high-Mn austenitic steels with Mn contents ranging from 15 to 25%. These high-Mn steels show promising low temperature mechanical properties and, in the near future, they are expected to replace expensive nickel (Ni)-containing steels used in LNG tankage and offshore structures [10-12]. The production of offshore structure and equipment often requires a welding process and they are subject to fail by fatigue process at the weld. It is therefore of practical importance to understand the fatigue crack propagation (FCP) behavior of high-Mn steels, particularly in the regime of low stress intensity factor range (ΔK) where the most of structure's life is spent. Previously, the authors reported the FCP behavior of Fe24Mn specimens in the region of BM, WM and FL at room temperature and 110 K [13]. The resistance to FCP of Fe24Mn specimens in the region of BM, WM and FL was greatly improved with decreasing temperature from 298 to 110 K [13]. The FCP rates of Fe24Mn in the region of WM and FL were comparable with each other at both 298 and 110 K, while the BM specimen showed slightly higher FCP rates than the WM and the FL specimen, particularly in near-threshold ΔK regime. Other than the increase in FCP resistance, the overall trend in the FCP behavior of Fe24Mn at 110 K was similar to that at 298 K.

Steels for offshore applications [14-16] require excellent resistance to FCP in corrosive environments since they are operated under fatigue loading in seawater environment. To improve the service life of offshore structures, a cathodic protection (CP) is often utilized [1,17-19], and several guidances for the CP levels for steel structure in seawater are available [1,19,20]. The CP potential required for full protection (i.e., corrosion rate reduced to insignificant level) of steel in seawater is widely considered to be around -850 mV_{SCE} [21]. The impressed current CP can result in hydrogen embrittlement (HE) which decreases the mechanical properties of high-strength steels, particularly at welds [1,22]. Due to the complexity of structures, it is often possible to have high negative values occurring in the vicinity of anodes more negative

*Corresponding author: sang@gnu.ac.kr

than -1,000 mV_{SCE} with the risk of HE and enhanced FCP, and more positive potentials than -750 mV_{SCE} at remote or shielded locations with the risk of localized corrosion [1]. It is therefore important to understand the effect of applied potential on the FCP behavior of steels in seawater. Limited information on near-threshold FCP data for high strength steels shows that an apparent increase in threshold value occurs with increased levels of CP compared with that in air at low R ratios [1,23-25]. Many studies have demonstrated that this behavior is due to crack wedging effects reducing the effective stress intensity range [1,19,26,27], and this mechanism is diminished [1] and the threshold values are similar to those in air at high R ratios [1,23,24].

In this study, the FCP behavior of Fe24Mn specimens in the region of BM and WM was investigated in artificial seawater under various applying potentials. The crack paths and fracture surfaces were documented by using a scanning electron microscope (SEM) to identify any morphological changes in fracture surface with different service environments. The FCP behavior of high-Mn austenitic steels was discussed based on the microstructural and the fractographic observations.

2. EXPERIMENTAL PROCEDURES

The butt-welded Fe24Mn plate with the thickness of 30 mm was supplied by POSCO (Pohang, Korea). The tensile properties of Fe24Mn steel at room temperature were reported in the reference [4]. For the micrographic observation, the specimens were polished and etched by using a 2% Nital solution for 20~50 sec. Figure 1 shows the optical micrographs of Fe24Mn steel documented in the region of (a) BM and (b) WM showing dendrite structure and columnar grain boundaries. As previously reported in the reference [13], an austenite single phase with equi-axed grains of average size of 38 μm was observed in the region of BM. In the region of WM, the typical dendritic structure with an average secondary dendrite arm spacing (SDAS) of 19 μm (Fig. 1(b)) and the columnar grains with the average size of 221 μm along the crack propagation direction (Fig. 1(c)) were observed.

The compact tension (CT) specimens were prepared from

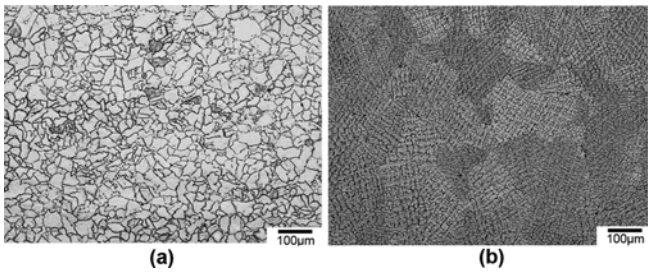

Fig. 1. The optical micrographs of Fe24Mn steel documented in the region of (a) BM and (b) WM showing dendrite structure and columnar grain boundaries.

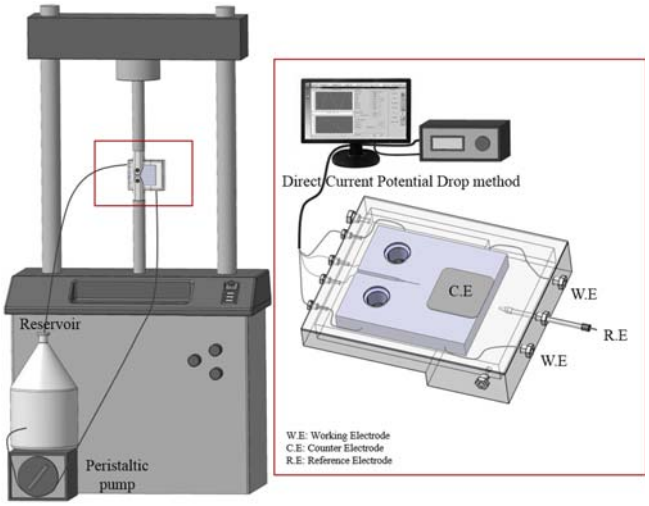

Fig. 2. The environmental cell used for polarizing the CT specimen in ASW during FCP test.

the BM with the L-T orientation and the WM of the butt-welded Fe24Mn steel plate for the FCP tests. The FCP tests were carried out on the CT specimens in flowing artificial seawater (ASW), which was made according to ASTM 1141 [28], at an R ratio of 0.1 with a sinusoidal frequency of 10 Hz in accordance with ASTM E647 [29] using a servo-hydraulic testing machine (Instron Model 8516). The CT specimen was polarized in ASW during fatigue test using an environmental cell shown in Fig. 2. The fatigue crack length was automatically measured by using a DCPD (direct current potential drop) method. The SEM analyses were conducted on the FCP tested specimens to examine any change in fracture mode with varying testing conditions. The FCP tested specimens in ASW were ultrasonically cleaned in distilled water for 20 min to remove any calcareous deposits on the fracture surface.

The linear polarization tests were conducted on the Fe24Mn specimen in ASW at 298 K at a scan rate of 1 mV/s. For the electrochemical tests, the samples were ground using an SiC paper up to # 2000, and the area exposed (0.13 cm^2) was controlled using electroplating tape. A three-electrode cell (a saturated calomel reference electrode (SCE), a Pt plate counter electrode and a working electrode) was used, and the electrochemical tests were carried out using a potentiostat (PAR Versarstat II model) [30]. Figure 3 shows the polarization curve of Fe24Mn specimen in the region of BM and WM, showing almost similar E_{corr} level of approximately -720 mV_{SCE} for both regions. Based on this E_{corr} value, the anodic potential of -600 mV_{SCE} and the CP potentials of -850 and -1,050 mV_{SCE} were applied in ASW for the present study.

The slow strain rate test (SSRT) method was utilized to evaluate the susceptibility of hydrogen embrittlement on the Fe24Mn specimen in ASW under CP potential of -1,050 mV_{SCE} at a strain rate of 1×10^{-6}/s on a constant extension rate test machine (R&B model, T07-025) in accordance with ASTM

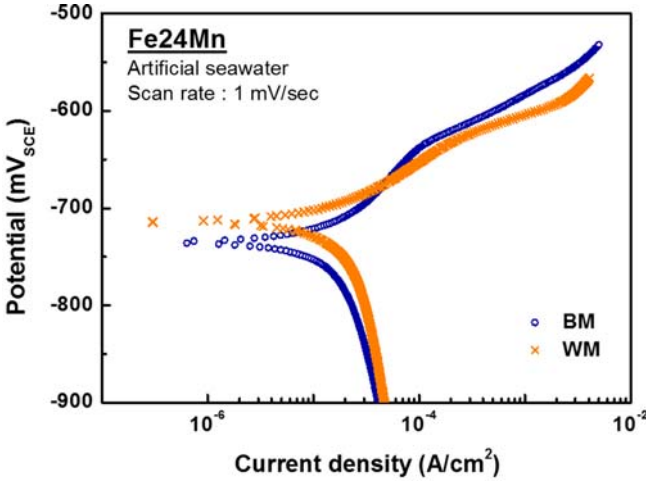

Fig. 3. The polarization curve of Fe24Mn specimen in the region of BM and WM tested in ASW at 298 K at a scan rate of 1 mV/s.

G129 [31]. For the SSRT, the smooth tensile specimens with a gauge length of 24 mm and a diameter of 4 mm were prepared from the plate parallel to rolling direction. As reference data, the SSRTs were performed in laboratory air at the same strain rate of 1×10^{-6}/s. The SEM fractographic analysis was also conducted on the SSRTed specimens to identify the mode of fracture.

3. RESULTS AND DISCUSSION

For the metals under fatigue loading in seawater environment, the fatigue mechanism is affected by the environmental variables, such as anodic dissolution and hydrogen embrittlement, as well as the mechanical variables [32-34]. The anodic dissolution mechanism involves the rupture of protective film at the crack tip and the subsequent repassivation of newly exposed fresh metal surface [35]. The FCP rates in corrosive environment is then controlled by the anodic dissolution rate of bare surface, the rate of repassivation, the rate of oxide film rupture and the mass transport rate of reactant to the dissolving surface [32-35]. To prevent the anodic dissolution, pipelines and offshore structures are often protected by a cathodic protection method with the potential ranging from -800 to -1,100 mV_{SCE} generally imposed [21,23]. The potentials above the proper range may however cause the embrittlement of metal by hydrogen generated at the surface and eventually increase the FCP rates [21].

Figure 4 shows the da/dN-ΔK curves of Fe24Mn BM specimen in air and ASW under the anodic applied potential of -600 mV_{SCE} and the CP potential of -850 and -1,050 mV_{SCE}, respectively. It was shown that the FCP rates of Fe24Mn BM increased in ASW under an anodic potential, as compared to those in air, along with a decrease in the near-threshold ΔK (ΔK_{th}) value. The ΔK_{th} value was, for example, 7.4 MPa√m at an applied potential of -600 mV_{SCE}, while it was 9.1 MPa√m

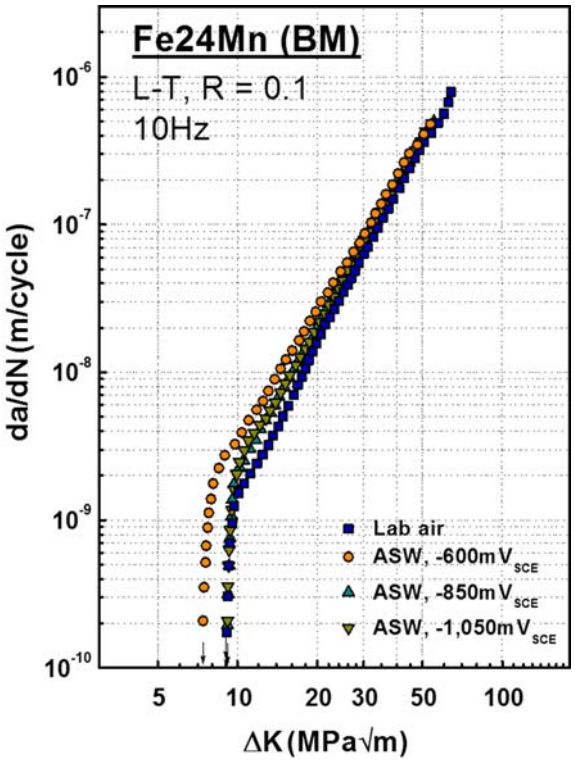

Fig. 4. The da/dN-ΔK curves of Fe24Mn BM specimen in air and ASW under the anodic applied potential of -600 mV_{SCE} and the CP potential of -850 and -1,050 mV_{SCE}, respectively.

in air. The present results clearly show the detrimental effect of anodic dissolution on the FCP behavior of Fe24Mn steel. With increasing ΔK, the FCP rates in ASW under anodic applied potential became similar to those in air. It is because the time to cause an environmental effect is not sufficient with the increase in FCP rates at high ΔK regime. For the Fe24Mn BM specimens tested in ASW under CP potentials of -850 and -1,050 mV_{SCE}, the FCP rates and the ΔK_{th} values were similar to those in air. Different CP potentials of -850 to -1,050 mV_{SCE} did not affect the FCP behavior in ASW, both showing similar ΔK_{th} values of around 9 MPa√m. The present study clearly demonstrated that the CP potential ranging from -850 to -1,050 mV_{SCE} worked to prevent the anodic dissolution during the FCP of Fe24Mn steel in seawater. No notable side effect of hydrogen embrittlement was observed in this CP potential range.

Figures 5, 6 and 7 show the SEM fractographs of the FCP tested Fe24Mn BM specimens in (a) air and ASW at (b) the anodic potential of -600 mV_{SCE}, and the CP potential of (c) -850 and (d) -1,050 mV_{SCE}, respectively, documented in the ΔK_{th} regime (Fig. 5) and at the ΔK of 30 (Fig. 6) and 50 MPa√m (Fig. 7). The crack propagation direction was from left to right. In the near-threshold ΔK regime, the slip deformation ahead of crack tip is crystallographic and blocked by the grain boundary. The transgranular cleavage facets are therefore

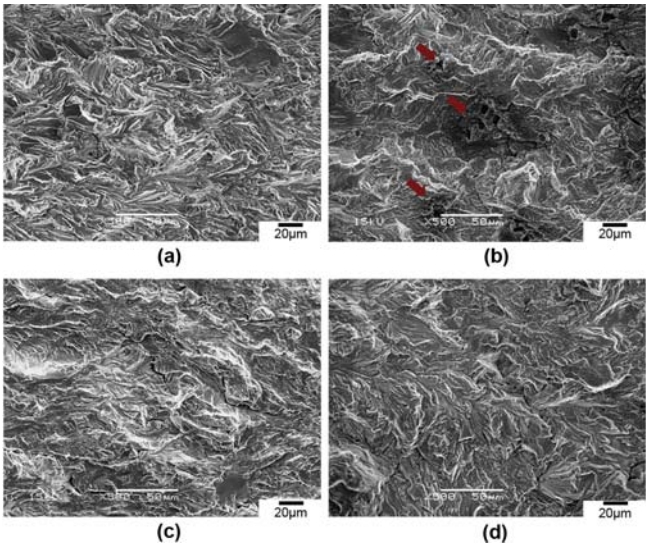

Fig. 5. The SEM fractographs of the FCP tested Fe24Mn BM specimens in (a) air and ASW at (b) the anodic potential of -600 mV_{SCE}, and the CP potential of (c) -850 and (d) -1,050 mV_{SCE}, respectively, documented in the ΔK_{th} regime.

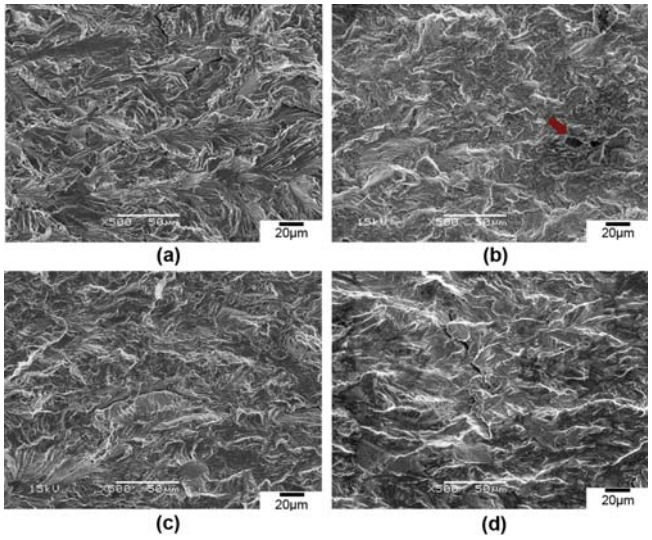

Fig. 6. The SEM fractographs of the FCP tested Fe24Mn BM specimens in (a) air and ASW at (b) the anodic potential of -600 mV_{SCE}, and the CP potential of (c) -850 and (d) -1,050 mV_{SCE}, respectively, documented at ΔK of 30 MPa$\sqrt{m}$.

generally smaller than the grain size in the near-threshold ΔK regime. In air, relatively fine transgranular facets with an average size of 26 μm were shown on the Fe24Mn specimen in the ΔK_{th} regime. Under the applied potential of -600 mV_{SCE} in ASW, basic fracture mode of transgranular faceting was not changed. Compared to that in air, several areas on the faceted fracture surface showed a sign of anodic dissolution (as indicated by arrows) in the ΔK_{th} regime. Probably due to the anodic dissolution, the facets were not as sharp as those observed in air (see Figs. 5(a) and 5(b)). The transgranular cleavage facet mode also prevailed for the Fe24Mn BM specimens tested in AWS under CP potentials. The close examination of fractographs showed that a subtle difference existed between those in air and ASW under CP potential (see Figs. 5(a), 5(c) and 5(d)). The size of facets tended to be relatively greater for the specimens tested in the hydrogen-generating environment. Such a trend was clearer at an applied CP potential of -1,050 mV_{SCE} in ASW, suggesting an encouraged transgranular cleavage faceting in hydrogen-generating environment. The applied CP potential generates hydrogen at the metal surface, and this hydrogen is absorbed and then transported by diffusion into the highly stressed region (plastic zone) at the crack tip [36,37]. Several hydrogen-assisted cracking mechanisms have been proposed to explain how hydrogen affects FCP rates, including (a) lattice decohesion mechanism, (b) surface adsorption mechanism and (c) hydrogen enhanced plasticity mechanism [38]. The lattice decohesion mechanism postulates that the hydrogen as a solute decreases the cohesive bonding forces between metal atoms, while the surface adsorption mechanism proposes that strongly absorbed hydrogen at the surface serves to lower the surface energy of the metal needed for crack extension [39,40]. Both mechanisms would increase the FCP rates, whichever is dominant, by embrittling the materials and reducing the driving force for crack extension. The hydrogen enhanced plasticity mechanism proposes that hydrogen assists the process of plastic flow by enhancing the dislocation mobility at the crack tip [41]. In contrast to previous hydrogen-assisted cracking mechanisms, it is argued that hydrogen in the lattice merely assists the fracture processes in the hydrogen enhanced plasticity mechanism [40,41]. The encouraged transgranular faceting mode in ASW under CP potentials suggested that the hydrogen enhanced plasticity mechanism served the dominant role in the present study. At ΔK of 30 MPa$\sqrt{m}$, the transgranular cleavage facet mode still prevailed for Fe24Mn BM specimen in air and in ASW under anodic and CP potentials. The macroscopically mode I crack advance perpendicular to the loading direction also began to be observed (Fig. 6). It is well known that, in the near-threshold regime, the scale of local plasticity (i.e., the plastic-zone size) approaches the scale of microstructural features, and measured FCP rates become less than an interatomic spacing per cycle, and a single shear mode of crack advance with associated mode II plus mode I displacements is encouraged [42]. With increasing ΔK, the slip deformation occurs on more than one slip plane in the plastic zone at the tip of crack which propagates macroscopically perpendicular to the loading direction. For the specimen tested in ASW under anodic potential of -600 mV_{SCE}, the area of anodic dissolution was significantly reduced. With further increase in ΔK to 50 MPa$\sqrt{m}$, the mode I crack extension prevailed along with fine striations (Fig. 7). As shown in Figs. 5 and 6, some sign of environmental attacks,

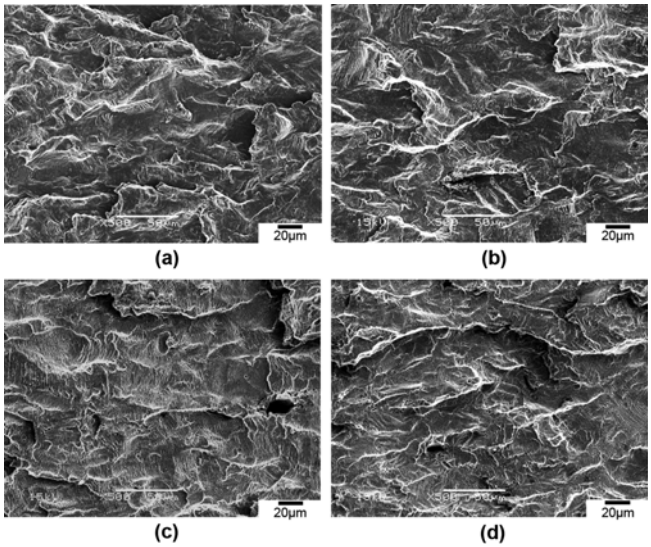

Fig. 7. The SEM fractographs of the FCP tested Fe24Mn BM specimens in (a) air and ASW at (b) the anodic potential of -600 mV_{SCE}, and the CP potential of (c) -850 and (d) -1,050 mV_{SCE}, respectively, documented at ΔK of 50 MPa√m.

including anodic dissolution on the fracture surface under anodic potential of -600 mV_{SCE} and the encouraged transgranular cleavage faceting in hydrogen-generating environment of applied potential of -1,050 mV_{SCE}, were observed in the near-threshold ΔK regime. Unlike those in the near-threshold ΔK regime, no difference in fracture mode was observed for the Fe24Mn BM specimens in different environments at ΔK to 50 MPa√m. It is since, at high ΔK regime, the crack growth is fast enough to suppress the detrimental effects in seawater environment.

For a clearer understanding on the possible hydrogen damage, the SSRTs were conducted on the Fe24Mn BM specimen in ASW under a CP potential of -1,050 mV_{SCE}. Figure 8 shows the stress-strain curves of the Fe24Mn BM specimens SSRTed in air and ASW at a strain rate of 1×10^{-6}/s. It was found that the tensile elongation decreased from 14.8% in air to 13.4%, while the ultimate tensile strength increased from 1,026 MPa to 1,103 MPa, in ASW under the CP potential of -1,050 mV_{SCE}. It has been proposed that the susceptibility to hydrogen embrittlement can be adequately expressed by the reduction ratio of tensile elongation between hydrogen-generating environment and benign environment [43-45]. The tensile elongation of Fe24Mn steel decreased from 14.8% in air to 13.4% in ASW under the CP potential of -1,050 mV_{SCE}, showing less than 10% reduction. Considering the SSRT results on structural metals, the effect of hydrogen was believed to be marginal in affecting the FCP behavior of the Fe24Mn specimens at a loading frequency of 10 Hz [43]. Based on the limited test result in Figure 8, the increase in tensile strength partially supported the hydrogen enhanced plasticity mechanism in the FCP behavior of Fe24Mn in seawater under CP potentials. Further

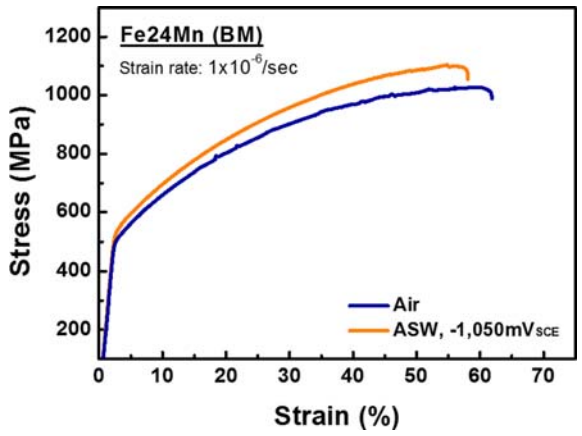

Fig. 8. The stress-strain curves of the Fe24Mn BM specimens SSRTed in air and ASW under the CP potential of -1,050 mV_{SCE} at a strain rate of 1×10^{-6}/s.

studies are required to confirm this notion. In the hydrogen generating environment, the dimples became shallower, indicating a reduced ductility. The present SSRT results suggested that the Fe24Mn steel is susceptible to hydrogen embrittlement in ASW under CP potential of -1,050 mV_{SCE}, but the effect is not as significant as to affect the FCP behavior. Indeed, the da/dN-ΔK curves in Fig. 5 show that the CP potentials of -850 to -1,050 mV_{SCE} in ASW suppress the anodic dissolution without causing hydrogen damage on Fe24Mn steel in seawater.

Figure 9 shows the da/dN-ΔK curves of Fe24Mn WM

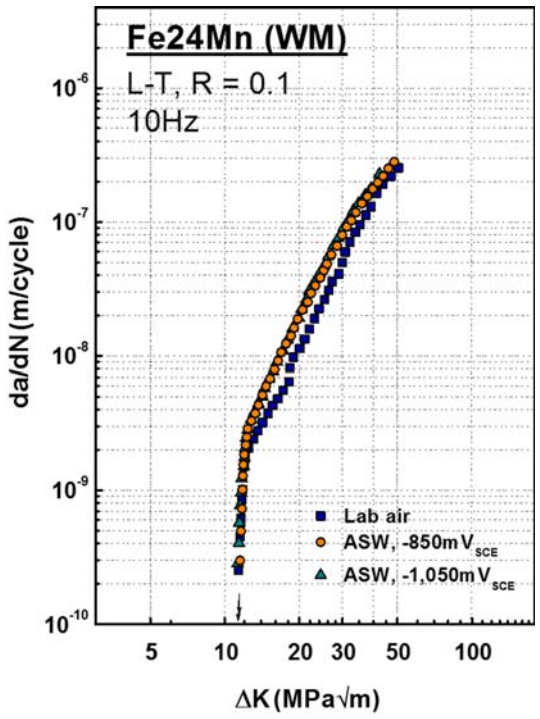

Fig. 9. The da/dN-ΔK curves of Fe24Mn WM specimens in air and ASW under the CP potential of -850 and -1,050 mV_{SCE}, respectively.

specimens in air and ASW under the CP potential of -850 and -1,050 mV_{SCE}, respectively. It was previously reported that the FCP rates of Fe24Mn WM and FL specimen in air were slightly lower than those of the BM specimens particularly in the near-threshold ΔK regime [13]. The FCP rates of metal weld have been reported to be generally lower, or comparable, to those of base metal, probably due to the compressive residual stress [13,46,47]. The slightly reduced FCP rates for the Fe24Mn WM and FL specimens than the BM specimen in low ΔK regime in air suggested that the effect of residual stress on the present specimens was marginal. The effect of residual stress on the FCP behavior of the Fe24Mn BM, WM and FL specimens would not be varied in seawater under cathodic applied potentials. For the Fe24Mn WM specimens, the mode of transgranular cleavage facet was also observed in the near-threshold ΔK and lower Paris' regimes. The ratio between the size of cleavage facet and the size of grain is an important variable determing the slip reversibility. Since the crystallographic extension of fatigue crack is blocked by grain boundary, the extent of strain localization depends on the grain size. Thus the smaller grain size tends to reduce the slip length and the slip reversibility, reducing the resistance to FCP in the near-threshold ΔK regime. The previous fractographic analysis suggested that the columnar grain boundaries for the Fe24Mn WM specimen, rather than interdendrite boundaries, played the same role as grain boundaries for the BM counterpart [13]. Many of the fatigue failure modes occurring in welded joints involve fatigue cracking from severe imperfections which are actually an inherent part of the joint. The present study showed that the FCP rates of the Fe24Mn WM specimens tested in air and ASW under CP potential of -850 and -1,050 mV_{SCE} were comparable with each other over the entire ΔK regime. It was therefore concluded that the CP potentials ranging from -850 to -1,050 mV_{SCE} also worked for the Fe24Mn weld.

Figures 10, 11 and 12 show the SEM fractographs of the FCP tested Fe24Mn WM specimens in (a) air and ASW under the CP potential of (b) -850 and (c) -1,050 mV_{SCE}, respectively, in the near-threshold ΔK regime (Fig.10) and at ΔK = 30 MPa√m (Fig. 11) and 50 MPa√m (Fig.12). The crack propagation direction was from left to right. As previously reported, the FCP tested Fe24Mn WM specimens in air showed the transgranular facets, the size of which was substantially greater than that of BM counterpart, in the near-threshold ΔK regime [13]. In this regime, the scale of local plasticity (i.e., the plastic-zone size) approaches microstructural size-scales, and measured growth rates become less than an interatomic spacing per cycle, indicating that crack advance is not occurring uniformly over the entire crack front [48]. A single shear mode of crack advance associated with mode II plus mode I displacements

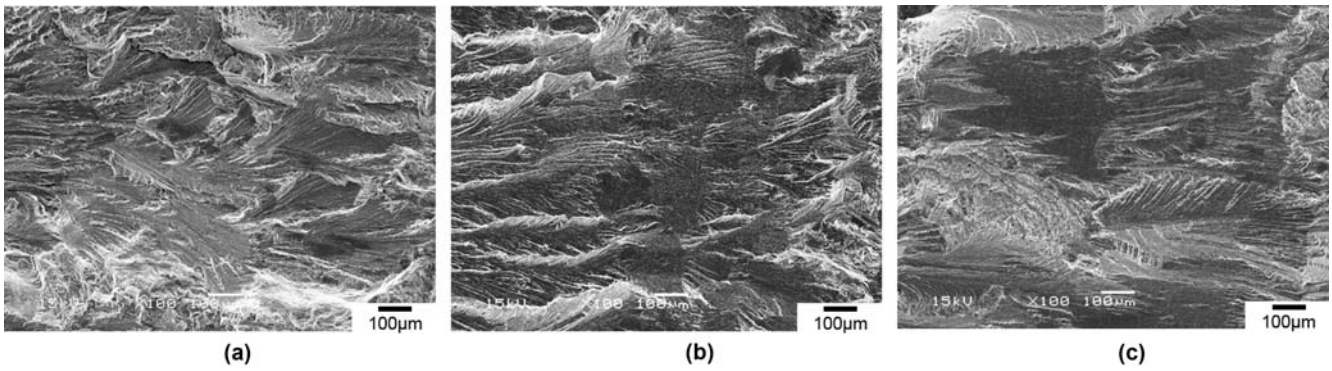

Fig. 10. The SEM fractographs of the FCP tested Fe24Mn WM specimens in (a) air and ASW under the CP potential of (b) -850 and (c) -1,050 mV_{SCE}, respectively, in the near-threshold ΔK regime.

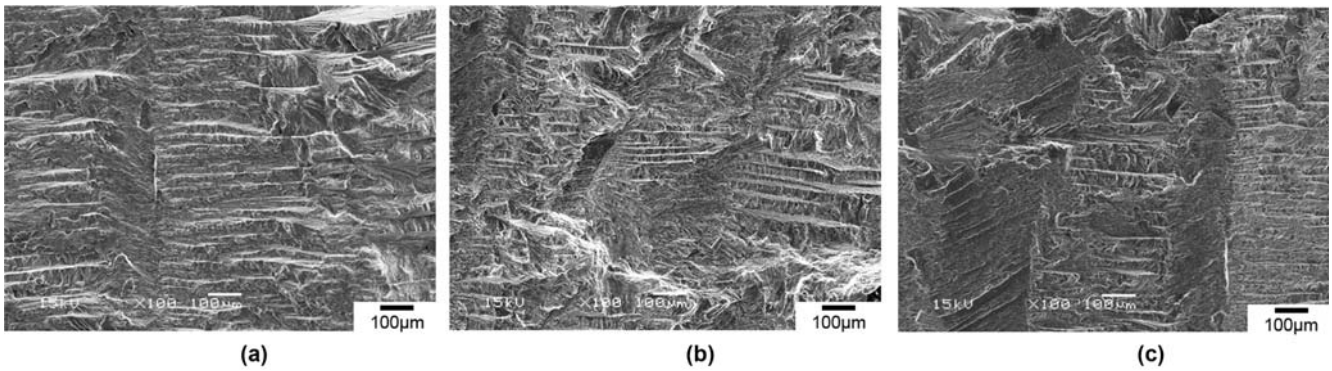

Fig. 11. The SEM fractographs of the FCP tested Fe24Mn WM specimens in (a) air and ASW under the CP potential of (b) -850 and (c) -1,050 mV_{SCE}, respectively, at ΔK = 30 MPa√m.

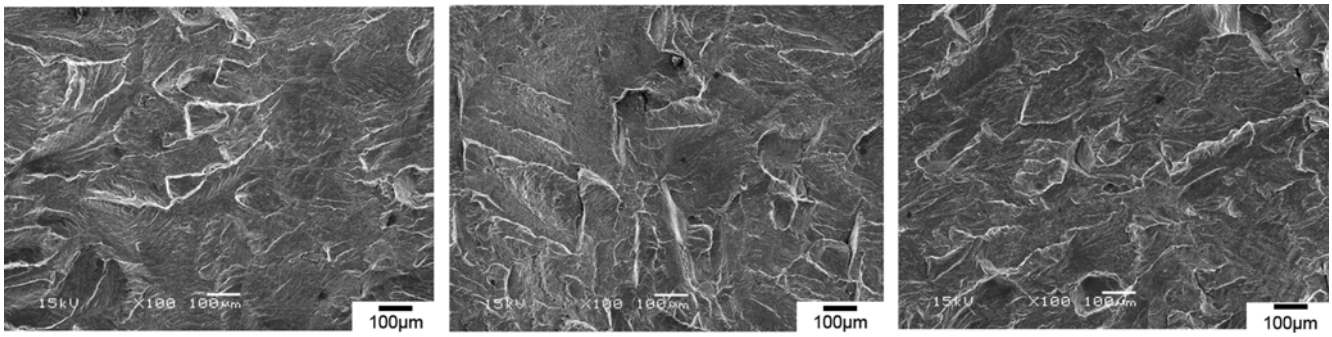

Fig. 12. The SEM fractographs of the FCP tested Fe24Mn WM specimens in (a) air and ASW under the CP potential of (b) -850 and (c) -1,050 mV_{SCE}, respectively, at $\Delta K = 50$ MPa$\sqrt{m}$.

Table 1. The slow strain rate test result for Fe24Mn BM specimens in air and ASW under the CP potential of -1,050 mV_{SCE} at a strain rate of 1×10^{-6}/s

Environments	Yield strength (MPa)	Ultimate tensile strength (MPa)	Tensile elongation (%)
Air	572	667	14.8
ASW/CP potential of -1,050 mV_{SCE}	565	663	13.3

is encouraged, and the fracture occurs along the lowest energy path of crystallographic plane. For the Fe24Mn WM specimens, the crystallographic advance of fatigue crack is blocked by the presence of columnar grain boundaries. With increasing ΔK, the slip deformation at the tip of crack occurs on more than one slip plane in the plastic zone at the tip of crack. For the Fe24Mn WM specimen in the Paris' regime, the mixed mode of crack advance along the interdendritic region and transgranular faceting was observed. Due to this interdendritic nature of crack advance, the step-like fracture surface was observed. The Fe24Mn WM specimens tested in ASW under two different CP potentials showed the similar fracture mode of transgranular faceting in the near-threshold ΔK regime, compared to those tested in air. It also appeared that the transgranular facets tended to be flatter for the specimens tested in the hydrogen-generating environment. Such a trend was clearer at an applied CP potential of -1,050 mV_{SCE} in ASW. The present result suggested that the hydrogen-enhanced plasticity mechanism was also applicable for the FCP behavior of Fe24Mn weld in ASW under CP potentials. Similar mixed mode of transgranular facet and step-like interdendritic crack extension was observed in intermediate ΔK of 30 MPa$\sqrt{m}$ for the WM specimens in ASW under CP potentials, as that for the BM specimen. At high applied ΔK of 50 MPa$\sqrt{m}$, the mode I crack extension prevailed along with fine striations for the Fe24Mn WM specimen. Again, no difference in fracture mode was observed for the Fe24Mn WM specimens with different CP potentials in ASW in this upper Paris' regime.

4. CONCLUSIONS

The FCP tests and the SSRTs were conducted on the Fe24Mn BM and WM specimens in air and ASW under various applied potentials, and the following conclusions were drawn.

(1) The near-threshold FCP resistance of Fe24Mn BM specimen was reduced in ASW under an anodic potential of -600 mV_{SCE}, as compared to those in air, while both environments showed similar FCP rates above $\Delta K = 20$ MPa$\sqrt{m}$.

(2) The CP potential of -850 and -1,050 mV_{SCE} suppressed the environmental effect of seawater on the FCP behavior of Fe24Mn BM and WM specimens, showing almost identical da/dN-ΔK curves in ASW.

(3) The FCP tests of Fe24Mn BM and WM specimens in both air and ASW under CP potentials of -850 and -1,050 mV_{SCE} shows similar fracture mode, suggesting that the present CP potentials in ASW suppressed the anodic dissolution without causing hydrogen damage on Fe24Mn steel in seawater.

(4) The SSRT in ASW under CP potential of -1,050 mV_{SCE} suggested that the Fe24Mn BM specimen steel was susceptible to HE, but the effect of hydrogen was marginal in affecting the FCP behavior of the Fe24Mn specimens at a loading frequency of 10 Hz.

ACKNOWLEDGMENTS

This work was supported by the National Research Foundation of Korea (NRF) grant funded by the Korea government (MSIP) (2011-0030058). This research was also supported by the Development of Drill Riser System Project (14-9807) of the KIGAM funded by the Ministry of Knowledge Economy of Korea.

REFERENCES

1. J. Billingham, J. V. Sharp, J. Spurrier, and P. J. Kilgallon, *Research Report 105*, pp.1-111, Health and Safety Executive (HAE) Books, Cranfield (2003).
2. NORSOK Standard M-001, Rev. 3, pp.7-23, Norway (2002).

3. D. T. Read and R. P. Reed, *Cryogenics* **21**, 415 (1981).
4. D. H. Jeong, S. G. Lee, W. K. Jang, J. K. Choi, Y. J. Kim, and S. S. Kim, *Metall. Trans. A* **44A**, 4601 (2013).
5. Z. Mei and J. W. Morris, Jr., *Metall. Trans. A* **21A**, 3137 (1990).
6. J. K. Kwon, H. Y. Lee, Y. J. Kim, and S. S. Kim, *Kor. J. Inst. Met. Mater.* **49**, 774 (2011).
7. N. B. Fredj and H. Sidhom, *Cryogenics* **46**, 439 (2006).
8. J. W. Morris, Jr., J. W. Chan, and Z. Mei, *Fourteenth International Cryogenic Engineering Conference and International Cryogenic Materials Conference*, p.1, Keiv, Ukraine (1992).
9. D. Y. Ryoo, S. C. Lee, Y. D. Lee, and J. Y. Kang, *Met. Mater. Int.* **7**, 1381 (2001).
10. R. Ogawa and J. W. Morris, Jr., *Fatigue at Low Temperatures*, ASTM STP 857, R.I. Stephens, ed., pp.47-59, American Society for Testing and Materials, Philadelphia (1985).
11. Q. Dai, R. Yang, and K. Chen, *Materials characterization*, **42**, 21 (1999).
12. T. Yokobori, I. Maekawa, Y. Tanabe, Z. Jin, and S. I. Nishida, *Fatigue at Low Temperatures*, ASTM STP 857, R. I. Stephens, ed., American Society for Testing and Materials, Philadelphia, 121 (1985).
13. D. H. Jeong, S. G. Lee, I. S. Seo, J. Y. Yoo, and S. S. Kim, *Met. Mater. Int.* **21**, 22 (2014).
14. W. Wang, Y. Shan, and K. Yang, *Mater. Sci. Eng. A*, **502**, 38 (2009).
15. S. Y. Shin, S. M. Hong, J. H. Bae, K. S. Kim, and S. H. Lee, *Met. Mater. Int.* **15**, 155 (2009).
16. Y. Wang, W. Zhao, H. Ai, X. Zhou, and T. Zhang, *Corros. Sci*. **53**, 2761 (2011).
17. J. K. Kwon, D. H. Ahn, D. H. Jeong, Y. J. Kim, N. S. Woo and S. S. Kim, *Korean J. Met. Mater.* ***52***, 757 (2014).
18. P. M. Scott, T. W. Therpe and D. R. V. Silvester, *Corros. Sci.* **23** 559 (1983).
19. C. Lindley and W. J. Rudd, *Mar. Struct*. **14**, 397 (2001).
20. NORSOK Standard M-503, Rev. 2, pp.5-9, Norway (1997).
21. H. Arup, *Corros. Eng. Sci. Tech.*, **26** 169 (1991).
22. M. Cabrini, S. Lorenzi, P. Marcassoli, and T. Pastore, *Corros. Rev.* **29**, 261 (2011).
23. R. N. King, *OTH96 511 Technology Report*, pp.1-43, Health and Safety Executive (HSE), Norwich, UK (1996).
24. R. N. King, A. Stacey, and J. V. Sharp, *15th International Conference Offshore Mechanics and Arctic Engineering*, p.341, Florence, Italy, (1996).
25. R. Murakami and W. G. Ferguson, *Fatigue Fract. Eng. Mater. Struct.* **9**, 477 (1987).
26. P. S. Pao, S. J. Gill, C. R. Feng, and K. K. Sankaran, *Scr. Mater.* **45**, 605 (2001).
27. A. K. Vasudevan and S. Suresh, *Metall. Trans. A* **13A**, 2271 (1982).
28. ASTM Standard D1141, *Standard Specification for Substitute Ocean Water*, Annual book of ASTM standards, 11.02. (1990).
29. ASTM Standard E647, *Standard Test Method for Measurement of Fatigue Crack Growth Rates*, Annual Book of ASTM Standards, vol. 03.01 (2002).
30. ASTM Standard G5, *Standard Reference Test Method for Making Potentiostatic and Potentiodynamic Anodic Polarization Measurements*, Annual Book of ASTM Standards, 03.02 (2002).
31. ASTM Standard G129, *Standard Practice for Slow Strain Rate Testing to Evaluate the Susceptibility of Metallic Materials to Environmentally Assisted Cracking*, Annual Book of ASTM Standards, 03.02 (2006).
32. Y. J. Kim, J. K. Kwon, D. H. Jeong, N. S. Woo, M. Goto, and S. S. Kim, *Met. Mater. Int.* Accepted (2014).
33. R. P. Wei, G. Shim, and K. Tanaka, *Embrittlement by Localized Crack Environment*, R. P Gangloff, ed., pp.243-263, TMS-AIME, Warrendale, Pennsylvania (1984).
34. C. Fong and D. Tromans, *Metall. Trans. A*, **19A**, 2753 (1988).
35. R. P. Gangloff, *Corrosion Tests and Standards - Application and Interpretation*, R. Babojan, ed. pp.253-271, ASTM International, West Conshohocken, Pennsylvania, 302 (2005).
36. J. H. Huang and C. J. Altsteller, *Metall. Trans. A*, **26A**, 1079 (1995).
37. I. M. Robertson, T. Tabata, W. Wei, F. Heubaum, and H. K. Birnbaum, *Scr. Met.* **18**, 841 (1984).
38. R. P. Gangloff, *Hydrogen Assisted Cracking of High Strength Alloys*, in Comprehensive Structural Inteqrity, I. Milne, R.O. Ritchie and B. Karihaloo, ed., pp.3-172, Elsevier Science, New York (2003).
39. D. P. Abraham and C. J. Altstetter, *Metall. Trans. A* **26**, 2849 (1995).
40. C. D. Beachem, *Metall. Trans. A* **3**, 437 (1972).
41. H. K. Birnbaum, *Mater. Sci. Eng. A* **176**, 191 (1994).
42. E. A. Starke and J. C. Williams, *in Fracture Mechanics, Perspectives and Directions, ASTM STP 1020*, p.184 R. P. Wei and R. P. Gangloff, eds., American Society for Testing and Materials, ,Philadelphia (1989).
43. P. Liang, X. Li, C. Dua, and X. Chen, *Mater. Des*. **30**, 1712 (2009).
44. Y. J. Kim, J. K. Kwon, Y. I. Jeong, N. S. Woo, and S. S. Kim, *Met. Mater. Int.* **19**, 19 (2013).
45. H. J. Lee, Y. J. Kim, Y. I. Jeong, and S. S. Kim, *Corros. Sci*. **55**, 10 (2011).
46. L.W. Tsay, T. S. Chern, C. Y. Gau, and J. R. Yang, *Int. J. Fatigue* **21**, 857 (1999).
47. C. H. Wang and Y. Chang, *Metall. Trans. A* **27A**, 3162 (1996).
48. R. O. Ritchie, *Met. Sci.* **11**, 368 (1977).